Continuum Mech. Thermodyn. (2015) 27:83–104
DOI 10.1007/s00161-013-0331-8

ORIGINAL ARTICLE

Matthieu Mazière · Samuel Forest

Strain gradient plasticity modeling and finite element simulation of Lüders band formation and propagation

Received: 31 July 2013 / Accepted: 7 December 2013 / Published online: 29 December 2013

Abstract An analytical solution of the problem of the propagation of a Lüders band in an isotropic strain gradient plasticity medium is provided based on a softening–hardening constitutive law. A detailed description is given of the plastic strain distribution in the finite size band front. The solution is shown to be harmonic in the band front and exponential in the band tail. Particular attention is paid to the conditions to be applied at the interface between both regions. This solution is then used to validate finite element simulations of the Lüders band formation and propagation in a plate in tension. The approach is shown to suppress the spurious mesh dependence exhibited by conventional finite element simulations of the Lüders behavior and to provide a finite width band front in agreement with the experimental observations from strain field measurements.

Keywords Lüders bands · Strain gradient plasticity · Finite element · Static strain ageing

1 Introduction

The well-known peak stress and Lüders plateau that occur during tensile tests on metallic materials at the elastic to plastic transition have been experimentally evidenced in the nineteenth century by Piobert [52] and Lüders [43]. This effect has been attributed by Cottrell [12] to the pinning of mobile dislocations by solute atoms in metals and alloys. This interaction of dislocations with solute atoms is called strain aging. If an aging treatment is carried out on a metallic specimen, solute atoms can diffuse close to dislocations. Compared to a non-aged material, a higher stress level is required to trigger plastic deformation. When the peak stress is overcome, the unpinning process of dislocations induces a softening of the material response followed by the propagation of a band of plastic deformation all along the specimen [44]. The propagation of this band is generally associated with a plateau at a constant stress level σ_p on the overall stress–strain curve. When the band has propagated along the specimen, the plateau ends up and the whole specimen is then homogeneously deformed, displaying conventional work-hardening. The strain corresponding to the end of the plateau regime is called the Lüders strain p_L. It is generally located at the intersection between the non-aged stress–strain curve and the plateau stress level. The peak stress level is mainly controlled by the aging time and temperature originally experienced by the material [4,5], while the Lüders strain can be affected by the grain size of the metal [16,41]. The Lüders bands have been experimentally observed using various techniques including strain field measurements [10,42,44]. The band front is generally found to be rather diffuse, involving a large number of grains. In this front zone, the plastic strain varies from the value p_L to zero.

The Lüders phenomenon can be simulated using various elastic–plastic models. The most simple approach amounts to define a bilinear softening and then hardening function of the cumulative plastic strain for the

Communicated by Andreas Öchsner.

M. Mazière · S. Forest (✉)
MINES ParisTech, Centre des Matériaux CNRS UMR 7633, BP 87, 91003 Evry Cedex, France
E-mail: samuel.forest@ensmp.fr

evolution of stress in the plastic domain [37,56,57]. Finite element simulations carried out on meshes of the full specimen show that the softening part that follows the yield point is responsible for strain localization in the form of a shear band starting from an existing defect or from the sample fillets. Once the Lüders strain is reached in the first localization zone, a band starts to propagate over the whole specimen. In the mean time, a stress plateau is observed on the overall stress–strain curve. The same behavior has been observed in simulations carried out using a nonlinear softening followed by hardening function that can be built from the sum of exponential functions [5,44]. A more sophisticated model based on the physical mechanisms underlying strain aging was proposed by McCormick, Kubin, Estrin [36,46,47]. This model is originally designed to simulate the Portevin–Le Chatelier effect but is also suitable for Lüders phenomenon, at least if the initial value of an additional internal variable called aging time is chosen suitably. The main advantage of this model is its ability to satisfactorily describe complex tensile experiments including heat treatments prior to, during, or after deformation, for instance to observe the influence of pre-straining on the stress peak level. This model has been successfully used in finite element simulations of the Lüders phenomenon in steels [6,29,30,44,58,59]. More elaborate constitutive equations are needed to better account for the coupling between aging phenomena and dislocation multiplication and interaction, see [26,33,48,50]. They have not yet been considered for systematic finite element simulations of sample behavior.

All these models induce strain localization when they are used in finite element simulations of metallic plates under simple tension. It is well known that conventional strain localization simulations are associated with spurious mesh dependence due to the loss of ellipticity of the set of partial differential equations [7]. Surprisingly, this fact has been overlooked in published results of simulations of the Lüders phenomenon. This is due to the fact that the hardening behavior that follows the softening regime in the constitutive law accounting for the Lüders effect restores the well posedness of the problem and that the mesh sensitivity is only transient. However, it has been demonstrated in [5,44,46] that conventional simulations of Lüders band formation and propagation are flawed by spurious mesh dependence, and that the plateau stress σ_p and Lüders strain p_L cannot be predicted accurately due to the presence of mesh-dependent oscillations on the overall curve. To get rid of mesh dependence, a regularization method can be introduced based on the introduction of strain gradient plasticity effects [1]. Motivations for such a regularization procedure originate from contributions in [2,32,38,50], which advocate that strain gradient plasticity effects play a significant role in the propagation of the Lüders band front.

In particular, the existing finite element simulations of Lüders behavior predict an abrupt drop of plastic strain at the band front lying between the plastically deformed and underformed zones of the sample during propagation. The band front thickness and shape are essentially controlled by mesh size [46] and mesh orientation [5,44]. In contrast, recent strain field measurements and physical observations of plastic activity suggest that the band front is a zone of finite size associated with inhomogeneous plastic deformation [42,44]. The band front extends over a significant number of grains, up to 100 [55]. The strain gradient plasticity models contain an intrinsic length that accurately accounts for the finite width of strain localization bands [9]. They can thus serve the two objectives of Lüders band simulation, namely numerical accuracy by means of mesh-independent results and physical relevance by means of a detailed description of the band front behavior. However, the relationship between the internal length introduced to regularize the model and the band front size observed in finite element simulation has never been derived for any of the models presented previously.

The aim of this article is to provide the framework for the accurate finite element simulation of Lüders band initiation and propagation in isotropic metals and alloys. For that purpose, a new analytical solution of the propagation of a Lüders band in an isotropic strain gradient continuum is derived. The solution provides a detailed description of the plastic strain distribution in the band front. A direct relation is given between the material parameters and the finite width of the band front, which has not been derived previously in the literature in the context of Lüders band propagation. The stress plateau σ_p and corresponding Lüders strain p_L are also derived as functions of the material parameters. The obtained analytical solution is then used to validate finite element simulations of the Lüders band initiation and propagation in a metallic plate in tension.

Section 2 is dedicated to the evidence of the strong mesh sensitivity of conventional simulations of the Lüders behavior with special attention to the effect of element orientation with respect to the tensile direction. Mesh sensitivity is illustrated both for two-dimensional and three-dimensional implicit finite element computations. For that purpose, a simple rate-independent elastoplasticity model based on von Mises criterion is used, including a non-monotonic bilinear hardening law. The theoretical formulation of the strain gradient plasticity model is given in Sect. 3. The Lüders band problem is then solved analytically based on this enhanced constitutive model in Sect. 4. Finally, finite element simulations using the regularized model are presented in Sect. 5 to outline the mesh objectivity of the results and to compare the results with the analytical solution.

The following notations are used for the mathematical objects of the models. First-, second-, and fourth-order tensors are, respectively, denoted by $\underline{\boldsymbol{a}}$, $\underset{\sim}{\boldsymbol{a}}$, and $\underset{\sim}{\underset{\sim}{\boldsymbol{a}}}$. Simple and double contractions are written $\cdot$ and $:$ respectively. The gradient operator is $\boldsymbol{\nabla}$. The divergence of a second-order tensor is written $\mathrm{div}\,\underset{\sim}{\boldsymbol{a}}$ and its Cartesian components are $a_{ij,j}$ with summation according to Einstein convention.

2 Evidence of mesh sensitivity in the simulation of Lüders band propagation

2.1 Material model

An elastoplastic material model is used in this work to model the Lüders band formation and propagation in a flat specimen under simple tensile loading conditions. The model formulation is limited to the small strain framework because it is suitable for the derivation of analytical solutions, as done in Sect. 4.

The strain rate $\dot{\underset{\sim}{\boldsymbol{\varepsilon}}}$ is split into elastic and plastic parts:

$$\dot{\underset{\sim}{\boldsymbol{\varepsilon}}} = \dot{\underset{\sim}{\boldsymbol{\varepsilon}}}^e + \dot{\underset{\sim}{\boldsymbol{\varepsilon}}}^p \tag{1}$$

The stress tensor is given by Hooke's law involving the fourth-order tensor $\underset{\sim}{\underset{\sim}{\boldsymbol{E}}}$ of elastic moduli:

$$\underset{\sim}{\boldsymbol{\sigma}} = \underset{\sim}{\underset{\sim}{\boldsymbol{E}}} : \underset{\sim}{\boldsymbol{\varepsilon}}^e \tag{2}$$

The yield function $f(\underset{\sim}{\boldsymbol{\sigma}}, R)$ involves the von Mises equivalent stress σ_{eq}:

$$f(\underset{\sim}{\boldsymbol{\sigma}}, R) = \sigma_{\mathrm{eq}}(\underset{\sim}{\boldsymbol{\sigma}}) - \sigma_M - R, \quad \sigma_{\mathrm{eq}} = \sqrt{\frac{3}{2}\underset{\sim}{\boldsymbol{s}} : \underset{\sim}{\boldsymbol{s}}} \tag{3}$$

where $\underset{\sim}{\boldsymbol{s}}$ is the deviatoric part of the stress tensor. The initial yield stress is σ_M and R accounts for work-hardening. The plastic flow follows from the normality rule:

$$\dot{\underset{\sim}{\boldsymbol{\varepsilon}}}^p = \dot{p}\underset{\sim}{\boldsymbol{N}}, \quad \underset{\sim}{\boldsymbol{N}} = \frac{\partial f}{\partial \underset{\sim}{\boldsymbol{\sigma}}} = \frac{3}{2}\frac{\underset{\sim}{\boldsymbol{s}}}{\sigma_{\mathrm{eq}}} \tag{4}$$

where $\dot{p} = \sqrt{\frac{2}{3}\dot{\underset{\sim}{\boldsymbol{\varepsilon}}}^p : \dot{\underset{\sim}{\boldsymbol{\varepsilon}}}^p}$ is the plastic multiplier and p is the cumulative plastic strain. Isotropic hardening is considered in the form of a function $R(p)$. The consistency condition during plastic loading provides the expression of the plastic multiplier in the form:

$$\dot{p} = \frac{\underset{\sim}{\boldsymbol{N}} : \underset{\sim}{\underset{\sim}{\boldsymbol{E}}} : \dot{\underset{\sim}{\boldsymbol{\varepsilon}}}}{\underset{\sim}{\boldsymbol{N}} : \underset{\sim}{\underset{\sim}{\boldsymbol{E}}} : \underset{\sim}{\boldsymbol{N}} + R'} \tag{5}$$

where $R'(p)$ is the derivative of the hardening function $R(p)$ with respect to p.

In order to simulate the Lüders band propagation in a specimen, the hardening law $R(p)$ must be a non-monotonic function of p, first displaying a softening and then a hardening behavior, as proposed in [20,56]. A bilinear evolution of $R(p)$ is chosen in this work:

$$R(p) = \sigma_m + H_1(p - p_m) - \sigma_M \quad \text{if } 0 \le p \le p_m \tag{6}$$

$$R(p) = \sigma_m + H_2(p - p_m) - \sigma_M \quad \text{if } p \ge p_m \tag{7}$$

where $H_1 < 0$ and $H_2 > 0$ are the two hardening moduli and p_m and σ_m are material parameters. The condition $R(p = 0) = 0$ implies that $H_1 = (\sigma_m - \sigma_M)/p_m$ so that the independent material parameters are $\sigma_M, \sigma_m, p_m, H_2$ or, equivalently, $\sigma_M, \sigma_m, H_1, H_2$. The corresponding evolution is plotted in Fig. 1.

2.2 Mesh sensitivity for two-dimensional specimens

The material model defined in the previous part has been used to simulate the propagation of a Lüders band in a $L = 96$ mm long and 12 mm large flat rectangular specimen. Simulations are carried out using the implicit finite element software Zset [8]. A Newton algorithm is used to solve global equilibrium under static conditions, and

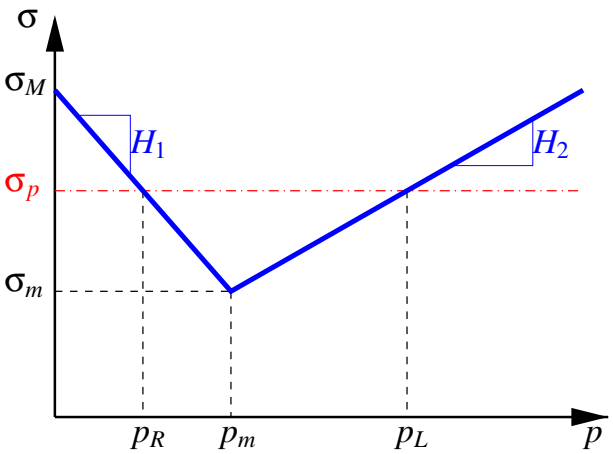

Fig. 1 Bilinear hardening law $\sigma = \sigma_M + R(p)$ used in the elastoplastic constitutive model

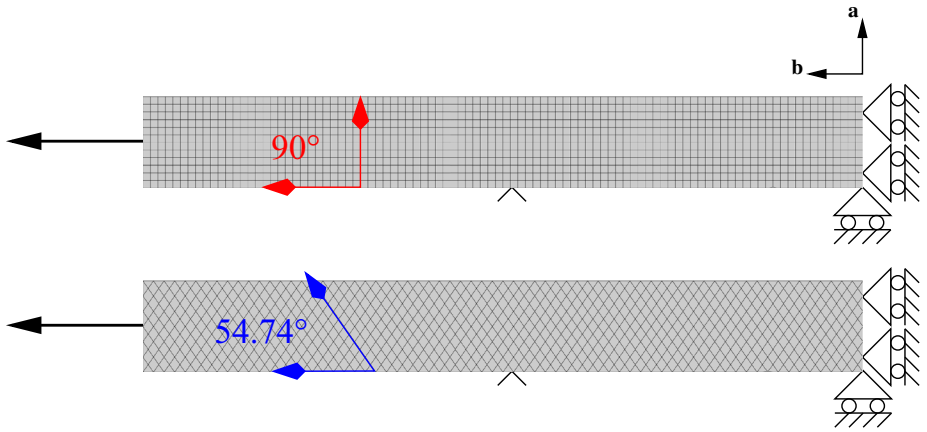

Fig. 2 90° and 54.74° oriented meshes used in this work to simulate the Lüders band propagation. Band nucleation is triggered by introducing a small geometrical imperfection denoted $\wedge$ on each mesh [37]

an implicit θ-method is resorted to in order to solve the set of constitutive differential equations at the Gauss point level [7].

The following illustrative material parameters have been used:

$$\sigma_m = 990\,\text{MPa},\ p_m = 0.01,\ H_1 = -1000\,\text{MPa},\ H_2 = 1000\,\text{MPa}$$

They are used here for the purpose of illustration and validation of the approach. More realistic parameters corresponding to a C-Mn steel displaying the Lüders phenomenon can be found in [44].

Two different 2D meshes with practically the same number of degrees of freedom (DOF), defined as twice the number of nodes in the mesh, have been investigated with two different element shapes and orientations. The first one is a regular mesh with quadrangular elements oriented parallel to the tensile direction (7,346 DOF). The second one is a regular mesh made of distorted quadrangular elements with edges making a constant angle of $\pm 54.74°$ with respect to the tensile axis. It contains 5,342 DOF. The chosen orientation of the lines of elements corresponds to the well-known orientation for plastic strain localization bands in isotropic elastoplastic materials, see [7,54]. The two meshes are plotted in Fig. 2. The elements are quadratic (8 nodes) with full integration. A small deformation plane stress formulation is used. All the simulations were carried out prescribing the vertical displacement of the top surface ($X_b = L$), while the displacement of the bottom surface ($X_b = 0$) is fixed to zero in the tensile direction (see Fig. 2).

The overall tensile response and the plastic strain field for the 90° oriented mesh are shown in Fig. 3. The overall stress can also be defined as the resulting force applied on the top surface divided by the thickness of the plate. The overall strain is taken as the total imposed relative displacement divided by the sample length. An

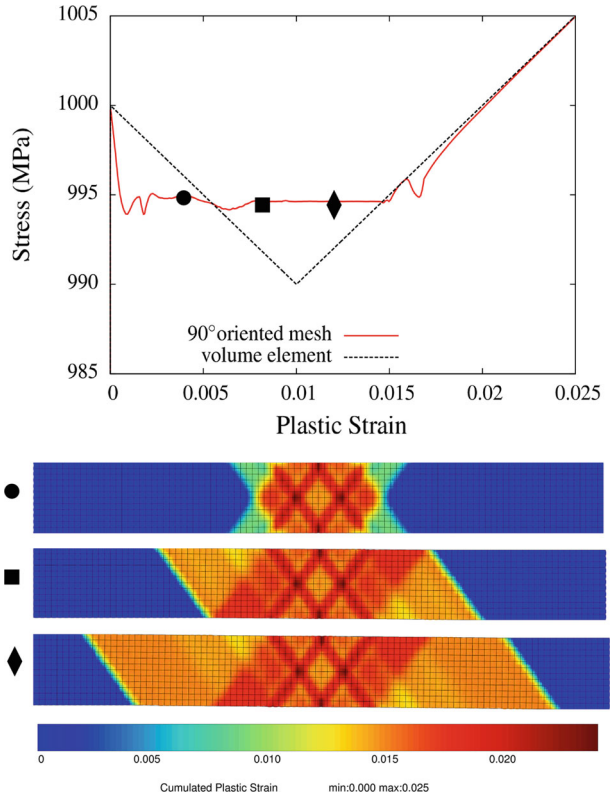

Fig. 3 Global stress versus plastic strain curve for the 90° oriented mesh. Maps of the cumulative plastic strain for an overall plastic strain equal to 0.004 (*bullet*), 0.008 (*black square*), and 0.012 (*black diamond*)

overall plastic strain can be defined after subtracting the overall stress divided by Young's modulus from the overall total strain. The overall curve displays an initial stress peak followed by an abrupt load drop, a plateau, and then hardening takes place after about 0.017 overall plastic strain. The curve displays a well-defined plateau stress called σ_p as observed in many experiments of the Lüders behavior [44]. The Lüders plateau is experimentally found to be more or less flat depending on the material and specimen shape. The simulated plateau stress value remains between σ_m and σ_M, and the minimum and maximum values reached by the volume element behavior according to the hardening law of Fig. 1. The bumps at the end of the plateau correspond to the contact of the band with one sample's end. The fields of cumulative plastic strain p at different loading steps in Fig. 3 show the clear spreading of a band-like deformation zone with two propagating fronts having an orientation of about $\pm 55°$ with respect to the tensile axis. Note also some crossing bands inside the plastic zone. The plastic strain rate is significant only at the band front the width of which is about 1 to 3 elements thick. The band front for this type of mesh is rather diffuse and can be shown to depend on the element size.

The results of the simulation carried out on the 54.74° oriented mesh show that the overall curve is strongly oscillating and that no plateau stress can be defined, see Fig. 4. The stress level oscillates between σ_m and σ_M during the whole propagation, even during band initiation at the early stage. During propagation, the plastic strain increases abruptly in a row of element, while nothing happens elsewhere in the specimen. The band front is then localized in a single row of element. The reason for such a difference in the finite element responses between both oriented meshes is due to the fact that the 54.74° oriented edges allow for discontinuities of the strain tensor as expected in a strain localization band. In contrast, for orientations different from 54.74°, a strict discontinuity of the strain is not possible, which results in a more diffuse band front. The severely oscillating behavior obtained with 54.74° oriented elements strongly differs from the experimental results of Lüders band propagation.

Simulations on irregular meshes based on free Delaunay meshing of the plates performed in [44] show results similar to that found for the 90° oriented mesh but, possibly, with slightly different values of σ_p.

As a result, the two-dimensional finite element simulations of the Lüders behavior are found to be strongly mesh dependent. The band front width depends on the element size and orientation. The plateau stress level depends on the element orientation. The 54.74° particular orientation leads to a spurious global stress–strain curve compared to the experimental results.

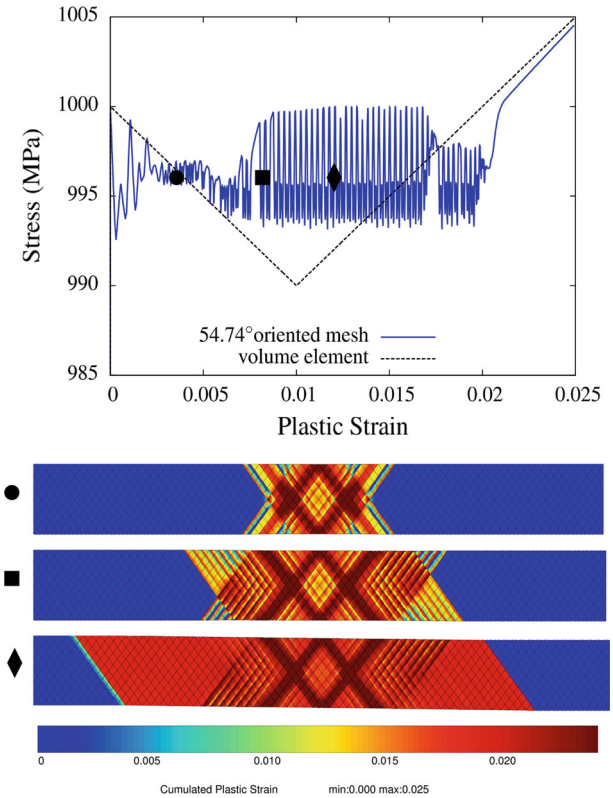

Fig. 4 Global stress versus plastic strain curve for the 54.74° oriented mesh. Maps of the cumulative plastic strain for a global plastic strain equal to 0.004 (*bullet*), 0.008 (*blacksquare*), and 0.012 (*black diamond*)

2.3 3D simulations: influence of specimen thickness

The previous simulations have been carried out within the plane stress assumption. It is well known that this type of simulation is more prone to strain localization than full 3D simulations [7]. Indeed, the sharp localization phenomenon observed for the 54.74° oriented mesh can be limited by the out-of-plane incompatibility of the strain jump in the thickness direction. In order to investigate the regularization that can be provided by this three-dimensional effect, simulations of the Lüders band propagation with the model presented in Sect. 2.1 have been carried out on four 3D specimens with different thickness: 3, 1, 0.3, 0.1 mm. The 54.74° oriented mesh has been extended in each case in the thickness direction with 3 layers of elements. The results of these four 3D simulations are presented in Fig. 5. They can be compared to the corresponding plane stress simulations presented in Fig. 4. For the thicker specimens (3 and 1 mm), the regularization due to geometrical effect is efficient: the stress remains on a plateau and the band front is smooth. For the thinner ones (0.3, 0.1 mm), results are close to the 2D plane stress simulations: the stress oscillates and the band front is sharp.

Accordingly, it can be said that spurious mesh dependence in the simulation of Lüders bands is observed irrespective of the space dimension and types of element. In particular, the band front thickness and the predicted plateau stress value are mesh dependent, which limits the confidence in the results of such simulations.

3 Strain gradient plasticity model

3.1 Motivation

The numerical results in Sect. 2 reveal a strong mesh dependence of the predicted plateau regime of the overall loading curves. Oscillations of various amplitudes are obtained that culminate in the case of element edges parallel to the band front. Such oscillations prevent us to determine a precise value of the plateau stress. On the other hand, the standard model predicts a sharp transition from the Lüders band to the plastically undeformed zone. This is in contradiction with strain field measurements indicating the existence of a smooth band front

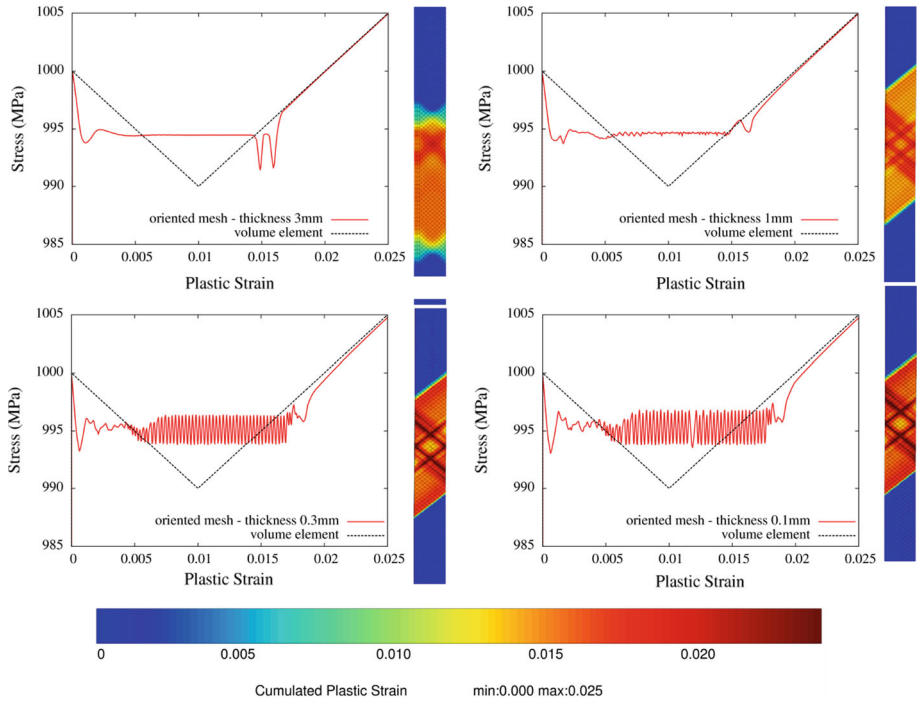

Fig. 5 Global stress versus plastic strain curves for a 3D 54.74° oriented mesh extended in the third direction. Maps of the local cumulative plastic strain for a global plastic strain equal to 0.008. Thickness of specimens is equal to 3 mm (*top left*), 1 mm (*top right*), 0.3 mm (*bottom left*), 0.1 mm (*bottom right*)

zone, typically corresponding to hundred times the grain size [10,42,44]. A smooth band front whose width can be controlled from specific material parameters is needed.

Both numerical and physical limitations can be solved by resorting to a strain gradient plasticity model as recommended in [2,32,50] for the simulation of the Lüders phenomenon. Strain gradient plasticity can be regarded as a mathematical regularization method that restores the well posedness of the boundary value problem in the presence of strain-softening effects [7,21]. On the other hand, it introduces an intrinsic length in the mechanical model, which reflects some aspects to the underlying microstructure of the material, here related to the cooperative deformation of grains of given size in a polycrystal.

The choice of the best-suited generalized continuum model for introducing a characteristic length in the constitutive framework remains heuristic in the sense that no micromechanical derivation is presented here to derive the appropriate continuum from microstructural considerations. The strain gradient theory introduced by Toupin and Mindlin [13,14,27,49] is a natural extension of the Cauchy continuum. In the context of plasticity, the microstructural effect can be limited to the plastic distortion, as done in [25,31] where the full gradient of the plastic strain is introduced in the constitutive modeling. This theory however leads to a computationally expensive model. In the isotropic case, it is sufficient to limit the strain gradient effect to the gradient of a scalar quantity like the cumulative plastic strain [60].

3.2 Theory

The general strain gradient plasticity framework is presented first in terms of balance and constitutive equations within the small strain framework. Special attention is given to the formulation of boundary and interface conditions that will be used in the analytical solution derived in the next sections. The theory is then specialized to the case of isotropic von Mises elastoplasticity.

3.2.1 Balance equations

The extension of the classical continuum plasticity framework is based on a generalization of the power density of internal forces. The degrees of freedom of the material point of the considered enhanced continuum are the

displacement vector $\underline{\boldsymbol{u}}$ and the cumulative plastic strain p regarded as independent and controllable variables. The theory then involves the gradient of the displacement field $\boldsymbol{\nabla}\underline{\boldsymbol{u}}$ and the gradient of the cumulative plastic strain $\boldsymbol{\nabla} p$.

The virtual power of internal forces of a subdomain $\mathcal{D} \subset \mathcal{B}$ of the body $\mathcal{B}$ is computed by means of a density $p^{(i)}$ that is assumed to depend on all virtual variations of the model variables

$$\mathcal{P}^{(i)}(\underline{\boldsymbol{v}}^*, \dot{p}^*) = \int_{\mathcal{D}} p^{(i)}(\boldsymbol{\nabla}\underline{\boldsymbol{v}}^*, \dot{p}^*, \boldsymbol{\nabla}\dot{p}^*)\,\mathrm{d}V \tag{8}$$

where $\underline{\boldsymbol{v}}^* = \underline{\dot{\boldsymbol{u}}}^*$ is a virtual velocity field, and $\dot{p}^*$ a virtual plastic strain rate field. The virtual power density of internal forces is taken as a linear form on the fields of virtual modeling variables

$$p^{(i)}(\boldsymbol{\nabla}\underline{\boldsymbol{v}}^*, \dot{p}^*, \boldsymbol{\nabla}\dot{p}^*) = \underset{\sim}{\boldsymbol{\sigma}} : (\boldsymbol{\nabla}\underline{\boldsymbol{v}}^*) + a\,\dot{p}^* + \underline{\boldsymbol{b}} \cdot \boldsymbol{\nabla}\dot{p}^* \tag{9}$$

The conjugate quantities in the power density are the simple stress tensor $\underset{\sim}{\boldsymbol{\sigma}}$, and the generalized stresses a (unit MPa) and $\underline{\boldsymbol{b}}$ (unit MPa mm). The generalized stresses are also called microstress and microforce according to [31]. The virtual power density of internal forces is invariant with respect to superimposed rigid body motion, so that $\underset{\sim}{\boldsymbol{\sigma}}$ is a symmetric second-order tensor [28].

The Gauss theorem is then applied to the power of internal forces

$$\begin{aligned}\int_{\mathcal{D}} p^{(i)}\,\mathrm{d}V = &\int_{\partial\mathcal{D}} \underline{\boldsymbol{v}}^* \cdot \underset{\sim}{\boldsymbol{\sigma}} \cdot \underline{\boldsymbol{n}}\,\mathrm{d}S + \int_{\partial\mathcal{D}} \dot{p}^*\,\underline{\boldsymbol{b}} \cdot \underline{\boldsymbol{n}}\,\mathrm{d}S \\ &- \int_{\mathcal{D}} \underline{\boldsymbol{v}}^* \cdot \operatorname{div}\underset{\sim}{\boldsymbol{\sigma}}\,\mathrm{d}V - \int_{\mathcal{D}} \dot{p}^*\,(\operatorname{div}\underline{\boldsymbol{b}} - a)\,\mathrm{d}V\end{aligned}$$

The form of the previous boundary integral dictates the form of the power of contact forces acting on the boundary $\partial\mathcal{D}$ of the subdomain $\mathcal{D} \subset \mathcal{B}$.

$$\mathcal{P}^{(c)}(\underline{\boldsymbol{v}}^*, \dot{p}^*) = \int_{\partial\mathcal{D}} p^{(c)}(\underline{\boldsymbol{v}}^*, \dot{p}^*)\,\mathrm{d}S \tag{10}$$

$$p^{(c)}(\underline{\boldsymbol{v}}^*, \dot{p}^*) = \underline{\boldsymbol{t}} \cdot \underline{\boldsymbol{v}}^* + a_c\dot{p}^* \tag{11}$$

where the simple traction $\underline{\boldsymbol{t}}$ (unit MPa) and double traction a_c (unit MPa mm) are introduced as surface densities of applied forces.

As a next step, the virtual power of external forces takes the form

$$\mathcal{P}^{(e)}(\underline{\boldsymbol{v}}^*, \dot{p}^*) = \int_{\mathcal{D}} p^{(e)}(\underline{\boldsymbol{v}}^*, \dot{p}^*)\,\mathrm{d}V \tag{12}$$

$$p^{(e)}(\underline{\boldsymbol{v}}^*, \dot{p}^*) = \underline{\boldsymbol{f}} \cdot \underline{\boldsymbol{v}}^* + \underset{\sim}{\boldsymbol{c}} : (\boldsymbol{\nabla}\underline{\boldsymbol{v}}^*) + a_e\dot{p}^* + \underline{\boldsymbol{b}}_e \cdot \boldsymbol{\nabla}\dot{p}^* \tag{13}$$

which involves the simple body forces $\underline{\boldsymbol{f}}$ (unit $\mathrm{N\,mm^{-3}}$), double body forces $\underset{\sim}{\boldsymbol{c}}$ ($\mathrm{N\,mm^{-2}}$), the generalized body forces a_e (unit $\mathrm{N\,mm^{-2}}$) and $\underline{\boldsymbol{b}}_e$ (unit $\mathrm{N\,mm^{-1}}$). The expression of the virtual power of external forces can be transformed into

$$\begin{aligned}\mathcal{P}^{(e)}(\underline{\boldsymbol{v}}^*, \dot{p}^*) = &\int_{\partial\mathcal{D}} \left(\underline{\boldsymbol{v}}^* \cdot \underset{\sim}{\boldsymbol{c}} \cdot \underline{\boldsymbol{n}} + \dot{p}^*\underline{\boldsymbol{b}}_e \cdot \underline{\boldsymbol{n}}\right)\mathrm{d}S \\ &- \int_{\mathcal{D}} \left(\underline{\boldsymbol{v}}^* \cdot (\operatorname{div}\underset{\sim}{\boldsymbol{c}} - \underline{\boldsymbol{f}})\,\mathrm{d}V + \dot{p}^*(\operatorname{div}\underline{\boldsymbol{b}}_e - a_e)\right)\mathrm{d}V\end{aligned} \tag{14}$$

In the static case, following [28], the principle of virtual power stipulates that

$$\mathcal{P}^{(i)}(\underline{\boldsymbol{v}}^*, \dot{p}^*) = \mathcal{P}^{(c)}(\underline{\boldsymbol{v}}^*, \dot{p}^*) + \mathcal{P}^{(e)}(\underline{\boldsymbol{v}}^*, \dot{p}^*), \quad \forall\underline{\boldsymbol{v}}^*, \forall\dot{p}^*, \forall\mathcal{D} \subset \mathcal{B} \tag{15}$$

which leads to

$$\int_{\partial\mathcal{D}} \underline{\boldsymbol{v}}^* \cdot (\underline{\boldsymbol{t}} - (\underset{\sim}{\boldsymbol{\sigma}} - \underline{\boldsymbol{c}}) \cdot \underline{\boldsymbol{n}}) + \dot{p}^* (a_c - (\underline{\boldsymbol{b}} - \underline{\boldsymbol{b}}^e) \cdot \underline{\boldsymbol{n}}) \, \mathrm{d}S$$
$$+ \int_{\mathcal{D}} \underline{\boldsymbol{v}}^* \cdot (\operatorname{div}(\underset{\sim}{\boldsymbol{\sigma}} - \underline{\boldsymbol{c}}) + \underline{\boldsymbol{f}}) + \dot{p}^* (\operatorname{div}(\underline{\boldsymbol{b}} - \underline{\boldsymbol{b}}_e) - a + a_e) \, \mathrm{d}V = 0 \tag{16}$$

The application of the principle of virtual power leads to the

– balance of momentum equation (static case)

$$\operatorname{div}(\underset{\sim}{\boldsymbol{\sigma}} - \underline{\boldsymbol{c}}) + \underline{\boldsymbol{f}} = 0, \quad \forall \underline{\boldsymbol{x}} \in \mathcal{B} \tag{17}$$

– balance of generalized momentum equation (static case)

$$\operatorname{div}(\underline{\boldsymbol{b}} - \underline{\boldsymbol{b}}_e) - a + a_e = 0, \quad \forall \underline{\boldsymbol{x}} \in \mathcal{B} \tag{18}$$

– boundary conditions

$$(\underset{\sim}{\boldsymbol{\sigma}} - \underline{\boldsymbol{c}}) \cdot \underline{\boldsymbol{n}} = \underline{\boldsymbol{t}}, \quad (\underline{\boldsymbol{b}} - \underline{\boldsymbol{b}}_e) \cdot \underline{\boldsymbol{n}} = a_c, \quad \forall \underline{\boldsymbol{x}} \in \partial\mathcal{B} \tag{19}$$

In the analytical work of Sect. 4, the external forces $\underline{\boldsymbol{f}}, \underline{\boldsymbol{c}}, a^e, \underline{\boldsymbol{b}}^e$ will be assumed to vanish. In that case, the balance and boundary conditions take the simpler form:

$$\operatorname{div} \underset{\sim}{\boldsymbol{\sigma}} = 0, \quad \operatorname{div} \underline{\boldsymbol{b}} - a = 0, \quad \forall \underline{\boldsymbol{x}} \in \mathcal{B} \tag{20}$$
$$\underset{\sim}{\boldsymbol{\sigma}} \cdot \underline{\boldsymbol{n}} = \underline{\boldsymbol{t}}, \quad \underline{\boldsymbol{b}} \cdot \underline{\boldsymbol{n}} = a_c, \quad \forall \underline{\boldsymbol{x}} \in \partial\mathcal{B} \tag{21}$$

Note that the form of the boundary conditions for strain gradient plasticity models is significantly less involved that the corresponding ones in Mindlin's strain gradient theory. This is due to the fact that the plastic strain tensor is generally not a compatible field, in contrast to the strain tensor. As a consequence, simple Dirichlet and Neumann conditions like (21) can be formulated that differ from the corresponding ones in the second gradient model, which involve normal and tangential derivatives of the fields and surface curvature [14].

3.2.2 Constitutive equations

The displacement field $\underline{\boldsymbol{u}}$ and the strain tensor are introduced. The latter is still decomposed into the elastic and plastic parts:

$$\underline{\boldsymbol{v}} = \dot{\underline{\boldsymbol{u}}}, \quad \underset{\sim}{\boldsymbol{\varepsilon}} = \frac{1}{2}(\nabla \underline{\boldsymbol{u}} + (\nabla \underline{\boldsymbol{u}})^T), \quad \underset{\sim}{\boldsymbol{\varepsilon}} = \underset{\sim}{\boldsymbol{\varepsilon}}^e + \underset{\sim}{\boldsymbol{\varepsilon}}^p \tag{22}$$

The state variables of the isothermal constitutive model are the elastic strain $\underset{\sim}{\boldsymbol{\varepsilon}}^e$, the cumulative plastic strain p, its gradient, and possibly some internal variables α for the sake of generality. The free energy density ψ and all stress tensors are assumed to be functions of the state variables:

$$\psi = \hat{\psi}(\underset{\sim}{\boldsymbol{\varepsilon}}^e, p, \alpha, \nabla p), \quad \underset{\sim}{\boldsymbol{\sigma}} = \hat{\underset{\sim}{\boldsymbol{\sigma}}}(\underset{\sim}{\boldsymbol{\varepsilon}}^e, p, \alpha, \nabla p)$$
$$a = \hat{a}(\underset{\sim}{\boldsymbol{\varepsilon}}^e, p, \alpha, \nabla p), \quad \underline{\boldsymbol{b}} = \hat{\underline{\boldsymbol{b}}}(\underset{\sim}{\boldsymbol{\varepsilon}}^e, p, \alpha, \nabla p)$$

where $\hat{\psi}$, $\hat{\underset{\sim}{\boldsymbol{\sigma}}}$, $\hat{a}$, and $\hat{\underline{\boldsymbol{b}}}$ are constitutive functionals.

The local form of the entropy principle for isothermal strain gradient plasticity takes the form [23,25]:

$$-\dot{\psi} + p^{(i)} \geq 0 \tag{23}$$

The isothermal Clausius–Duhem inequality is derived

$$\left(\underset{\sim}{\boldsymbol{\sigma}} - \frac{\partial \hat{\psi}}{\partial \underset{\sim}{\boldsymbol{\varepsilon}}^e}\right) : \dot{\underset{\sim}{\boldsymbol{\varepsilon}}}^e + \left(a - \frac{\partial \hat{\psi}}{\partial p}\right) \dot{p} + \left(\underline{\boldsymbol{b}} - \frac{\partial \hat{\psi}}{\partial \nabla p}\right) \cdot \nabla \dot{p} + \underset{\sim}{\boldsymbol{\sigma}} : \dot{\underset{\sim}{\boldsymbol{\varepsilon}}}^p - \frac{\partial \hat{\psi}}{\partial \alpha} \dot{\alpha} \geq 0 \tag{24}$$

The following state laws are adopted:

$$\underset{\sim}{\boldsymbol{\sigma}} = \frac{\partial \hat{\psi}}{\partial \underset{\sim}{\boldsymbol{\varepsilon}}^e}, \quad \underline{\boldsymbol{b}} = \frac{\partial \hat{\psi}}{\partial \nabla p} \tag{25}$$

meaning that the generalized stress is assumed to be associated with a non-dissipative process. Dissipative strain gradient contributions can be introduced but they are not necessary for the purpose of this work [21]. The thermodynamic forces associated with the internal variables α and to the degree of freedom p are

$$X = \frac{\partial \hat{\psi}}{\partial \alpha}, \quad R = \frac{\partial \hat{\psi}}{\partial p} \tag{26}$$

The residual dissipation rate is then given by

$$D^{res} = \underset{\sim}{\boldsymbol{\sigma}} : \dot{\underset{\sim}{\boldsymbol{\varepsilon}}}^{p} + (a - R)\dot{p} - X\dot{\alpha} \geq 0 \tag{27}$$

For the formulation of the yield criterion, an equivalent stress measure σ_{eq} is introduced such that

$$\underset{\sim}{\boldsymbol{\sigma}} : \dot{\underset{\sim}{\boldsymbol{\varepsilon}}}^{p} = \sigma_{\text{eq}}\dot{p} \tag{28}$$

The residual dissipation can be rearranged into

$$D^{res} = (\sigma_{\text{eq}} + a - R)\dot{p} - X\dot{\alpha} \geq 0 \tag{29}$$

At this stage, in the case of rate-independent plasticity, a yield function $f(\underset{\sim}{\boldsymbol{\sigma}}, R - a, X)$ is introduced. The principle of maximum dissipation rate is adopted and exploited using the Lagrangian function:

$$\Phi(\underset{\sim}{\boldsymbol{\sigma}}, R - a, X) = D^{res} - \lambda f(\underset{\sim}{\boldsymbol{\sigma}}, R - a, X) \tag{30}$$

where λ is a Lagrange multiplier. The extremum of Φ under the constraint $f = 0$ leads to the normality rule for plastic flow and to the hardening laws:

$$\dot{\underset{\sim}{\boldsymbol{\varepsilon}}}^{p} = \lambda \frac{\partial f}{\partial \underset{\sim}{\boldsymbol{\sigma}}}, \quad \dot{p} = -\lambda \frac{\partial f}{\partial (R - a)}, \quad \dot{\alpha} = -\lambda \frac{\partial f}{\partial X} \tag{31}$$

3.2.3 Isotropic gradient elastoplasticity

The specific constitutive equations used in this work are now specified. The free energy density is composed of three terms: the stored elastic energy density, the stored energy due to hardening, called $\psi_p(p)$, and the energy density associated with the gradient of cumulative plastic strain. The first and last contributions are assumed to be quadratic, which provides the most simple strain gradient plasticity model:

$$\psi(\underset{\sim}{\boldsymbol{\varepsilon}}^{e}, p, \nabla p) = \frac{1}{2}\underset{\sim}{\boldsymbol{\varepsilon}}^{e} : \underset{\sim}{\underset{\sim}{\boldsymbol{E}}} : \underset{\sim}{\boldsymbol{\varepsilon}}^{e} + \psi_p(p) + \frac{1}{2}\nabla p \cdot \underset{\sim}{\boldsymbol{A}} \cdot \nabla p \tag{32}$$

The tensor of elastic moduli was introduced in Eq. (2). Higher-order moduli are introduced in the form of the second-rank tensor $\underset{\sim}{\boldsymbol{A}}$ (unit MPa mm^2). The state laws follow from (25) and (26):

$$\underset{\sim}{\boldsymbol{\sigma}} = \underset{\sim}{\underset{\sim}{\boldsymbol{E}}} : \underset{\sim}{\boldsymbol{\varepsilon}}^{e}, \quad R(p) = \frac{\partial \psi_p}{\partial p}, \quad \underline{\boldsymbol{b}} = \underset{\sim}{\boldsymbol{A}} \cdot \nabla p \tag{33}$$

The potential ψ_p is chosen such that its derivative provides the hardening law (6–7). For simplicity, no internal variable α is used here. As a consequence, the balance of generalized momentum (20) provides the following partial differential equation, after substitution of the state laws for a homogeneous material:

$$a = \operatorname{div} \underline{\boldsymbol{b}} = \operatorname{div}(\underset{\sim}{\boldsymbol{A}} \cdot \nabla p) = \underset{\sim}{\boldsymbol{A}} : (\nabla \otimes \nabla p) = A\nabla^2 p \tag{34}$$

The higher-order modulus A is the single additional material parameter introduced by strain gradient plasticity in the case of material isotropy, $A_{ij} = A\delta_{ij}$. The higher-order stress a is then linearly related to the Laplace of cumulative plastic strain.

The yield function is chosen in the form:

$$f(\underset{\sim}{\boldsymbol{\sigma}}, R - a, X) = \sigma_{\text{eq}} - \sigma_M - R(p) + a \tag{35}$$

where σ_M is the initial yield stress and σ_{eq} is the same equivalent stress measure as in (3). The normality rule (31) gives:

$$\dot{p} = \lambda, \quad \underset{\sim}{\dot{\boldsymbol{\varepsilon}}}^p = \dot{p}\frac{\partial f}{\partial \underset{\sim}{\boldsymbol{\sigma}}}, \quad \sigma_{\text{eq}} = \underset{\sim}{\boldsymbol{\sigma}} : \frac{\partial f}{\partial \underset{\sim}{\boldsymbol{\sigma}}} \tag{36}$$

The yield condition $f = 0$

$$\sigma_{\text{eq}} = \sigma_M + R - a = \sigma_M + R(p) - A\nabla^2 p \tag{37}$$

shows that p is solution of a partial differential equation in the plastic domain [39,40]. So does the plastic multiplier $\dot{p}$ when the consistency condition $\dot{f} = 0$ is enforced. Equation (37) coincides with the well-known Aifantis strain gradient plasticity model [1,2], derived here in the context of thermodynamically consistent rate-independent elastoplasticity [22].

Solving the yield condition as a partial differential equation is a cumbersome numerical task, which requires the tracking of the boundary of the spatial domain undergoing plastic loading [39]. An alternative method for the numerical implementation of strain gradient plasticity is to resort to the micromorphic approach, which introduces an additional degree of freedom constrained to be close to the cumulative plastic strain by means of a penalty term in the free energy density, see [3,15,17,21,44,60]. The micromorphic model recalled in appendix 6 was implemented in the finite element code Zset using an implicit Newton global algorithm and an implicit θ-method for the integration of differential equations at each Gauss point [44,46].

4 Analytical solution for Lüders band propagation

An analytical solution for the propagation of a Lüders band is derived in this section using the strain gradient plasticity model presented in Sect. 3.2. The boundary value problem is formulated in the first subsection, special attention being paid to boundary conditions and interface conditions at the band front. Then, Eq. (37) is solved successively in the band front and in the band tail to compute the spatial distribution of the cumulative plastic strain p. Analytical expressions of the band front size and of the Lüders plateau stress are provided. Finally, the rate form of Eq. (37) is investigated in order to compute the analytical spatial distribution of the plastic strain rate $\dot{p}$.

4.1 Boundary value problem and interface conditions

A single Lüders band propagating under tensile loading in an infinite solid is investigated in this section, see Fig. 6. Far from sample boundaries, a band front zone can be defined as a material strip bounded, on one side, by a planar interface with normal vector $\underline{\boldsymbol{n}}$ separating the plastically undeformed part of the sample from the plastically deformed one and, on the other side, by a planar interface separating the band front zone from the band tail, which is the zone where plastic flow already occurred but is not significant any more. The finite thickness Y_f of this band front zone will be determined from the analysis. The specimen coordinate frame $(\boldsymbol{a}, \boldsymbol{b})$ is oriented along and perpendicular to the tensile axis. A new local frame $(O, \boldsymbol{X}, \boldsymbol{Y})$ is introduced and related to the band geometry, with X parallel to the band front. This moving coordinate frame is such that:

1. The cumulative plastic strain p does not depend on the coordinate X:

$$p(X, Y) = p(Y) \tag{38}$$

$$\nabla^2 p = \frac{\partial^2 p}{\partial X^2} + \frac{\partial^2 p}{\partial Y^2} = \frac{\mathrm{d}^2 p}{\mathrm{d}Y^2} = p'' \tag{39}$$

2. The plane $Y = 0$ is at each time located at the interface between the band front and the band tail.

The orientation $\underline{\boldsymbol{n}}$ of the band is known from the standard bifurcation analysis corresponding to the prediction of shear banding for isotropic plasticity [7]. The vector $\underline{\boldsymbol{n}}$ is oriented at 35.26° from the tensile axis. This analysis is still valid in the context of strain gradient plasticity.

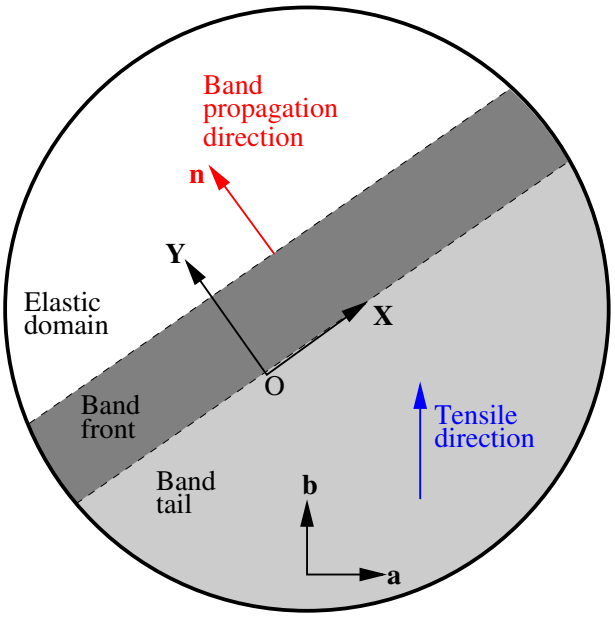

Fig. 6 Propagation of a single Lüders band in an infinite solid. Definition of the coordinate frame associated with the band propagation

4.2 Analytical solution for the distribution of plastic strain p

In the coordinate frame (O, X, Y), assuming plastic loading, Eq. (37) becomes:

$$\sigma_{\text{eq}} = \sigma_m + H_i(p - p_m) - Ap'' = \sigma_p \tag{40}$$

where σ_p is the plateau stress level defined in Fig. 1. The modulus H_i can take the values H_1 or H_2 depending on whether the material point is in the softening or hardening regime of Fig. 1. This equation is solved separately in the three different regions illustrated in Fig. 6: the band tail, the band front, and the elastic domain.

In the band tail, i.e., for $Y \leq 0$, the material points are in the hardening regime $p \geq p_m$. Then, $H_i = H_2$ is positive and the solution of Eq. (40) is exponential. When $Y \to -\infty$, the cumulative plastic strain p tends to a limit value p_L, the Lüders strain defined in Fig. 1.

In the band front, i.e., for $0 \leq Y \leq Y_f$, Y_f being the band front thickness, the material points experience softening, i.e., $0 \leq p \leq p_m$. Then, $H_i = H_1$ is negative and the solution of Eq. (40) is harmonic. The cumulative plastic strain p and its gradient p' remain continuous at $Y = 0$. We have $p(0) = p_m$ since H_i switches from H_2 in $Y < 0$ to H_1 for $0 < Y \leq Y_f$.

The continuity of p' at the interface originates from the fact that the generalized traction $a_c = \underline{\boldsymbol{b}} \cdot \underline{\boldsymbol{n}} = Ap'$, according to (21) and (25), is transmitted at any interface, as the usual traction $\underline{\boldsymbol{t}}$ does.

In the elastic domain, i.e., for $Y \geq Y_f$, there is no plastic deformation and $p = p' = 0$. The cumulative plastic strain p and its gradient p' are continuous at $Y = Y_f$, so that $p(Y_f) = 0$ and $p'(Y_f) = 0$.

A schematic representation of solution $p(Y)$ is drawn in Fig. 7. The six boundary and interface conditions provide the complete solution in each domain, the expression of the uniform tensile stress σ_p, and the band thickness Y_f as functions of material parameters σ_m, p_m, H_1, H_2, and A.

Solution in the band tail

In the band tail, the Eq. (40) becomes:

$$\sigma_{\text{eq}} = \sigma_m + H_2(p - p_m) - Ap'' = \sigma_p \tag{41}$$

which provides the differential equation:

$$p'' - w_2^2\, p = -w_2^2\, p_L, \quad \text{with} \quad w_2 = \sqrt{\frac{H_2}{A}} \tag{42}$$

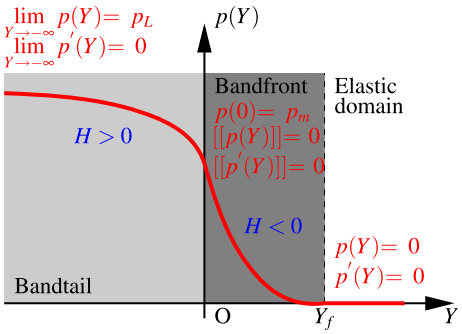

Fig. 7 Schematic representation of the solution $p(Y)$ of equation (40) and boundary conditions used to solve this equation. An exponential branch in the band tail is connected to a sinus branch in the band front

ω_2 being the inverse of a characteristic length of the model. The general form of the solution of this equation is

$$p(Y) = \alpha_2 \exp(w_2 Y) + \beta_2 \exp(-w_2 Y) + p_L \tag{43}$$

The integration constants α_2 and β_2 are determined after considering the limit at $-\infty$ and the interface condition at $Y = 0$:

$$p \text{ remains finite for } Y \to -\infty \Rightarrow \beta_2 = 0 \tag{44}$$

$$p(0) = p_m \Rightarrow \alpha_2 = p_m - p_L \tag{45}$$

The complete solution then is

$$p(Y) = (p_m - p_L) \exp\left(\sqrt{\frac{H_2}{A}} Y\right) + p_L \tag{46}$$

Solution in the band front

In the band front, Eq. (40) becomes

$$\sigma_{\text{eq}} = \sigma_m + H_1(p - p_m) - A p'' = \sigma_p \tag{47}$$

which provides the differential equation:

$$p'' + w_1^2 \, p = w_1^2 \, p_R \quad \text{with} \quad w_1 = \sqrt{-\frac{H_1}{A}} \tag{48}$$

The general form of the solution of this equation is

$$p(Y) = \alpha_1 \cos(w_1 Y) + \beta_1 \sin(w_1 Y) + p_R \tag{49}$$

where p_R is defined in Fig. 1. The integration constants α_1 and β_1 are determined by means of the interface equations at $Y = 0$:

$$\text{continuity of } p \Rightarrow \alpha_1 = p_m - p_R \tag{50}$$

$$\text{continuity of } p' \Rightarrow \beta_1 = \frac{w_2}{w_1}(p_m - p_L) \tag{51}$$

The complete solution then is

$$p(Y) = (p_m - p_R) \cos(w_1 Y) + \frac{w_2}{w_1}(p_m - p_L) \sin(w_1 Y) + p_R \tag{52}$$

The interface conditions at $Y = Y_f$ provide the expressions of the band front thickness Y_f and the plateau stress σ_p:

$$p(Y_f) = 0 \Rightarrow Y_f = \sqrt{-\frac{A}{H_1}}\left(\pi - \arctan\left(\sqrt{-\frac{H_1}{H_2}}\right)\right) \tag{53}$$

$$p'(Y_f) = 0 \Rightarrow p_L = p_R\left(1 + \sqrt{1 - \frac{H_1}{H_2}}\right) \tag{54}$$

$$\sigma_p = \frac{(\sigma_m - H_1 p_m) - (\sigma_m - H_2 p_m)\left(1 - \sqrt{1 - \frac{H_1}{H_2}}\right))}{\sqrt{1 - \frac{H_1}{H_2}}} \tag{55}$$

As expected, the band front thickness Y_f is a function of the higher-order modulus A. Using the values of material parameters values from Sect. 2, the analytical value of the plateau stress is $\sigma_p = 994\,\text{MPa}$.

4.3 Relation to Maxwell's rule

Maxwell's equal area rule is widely used for thermodynamical applications [45]. In some physical situations, the isothermal evolution in the pressure–volume phase diagram of a fluid can be non-monotonic displaying a S-shape, similarly to Fig. 1, the decreasing–increasing part actually being unstable. The non-monotonic material response is then replaced by an horizontal line at an equilibrium pressure level defined by the Maxwell equal area rule. The same construction can be applied to solids undergoing phase transformation or localized deformation due to the existence of non-convex potentials as shown in [34,38].

We show in this part that the analytical Lüders plateau stress evaluated from Eq. (55) also follows from such a Maxwell construction. The strain values p_R and p_L are, respectively, defined as the plastic strains for which the function $\sigma_M + R(p)$ intersects the Lüders plateau in the softening and hardening regimes, respectively:

$$\sigma_p - \sigma_m = H_1(p_R - p_m) = H_2(p_L - p_m) \Longrightarrow p_R = p_m + \frac{H_2}{H_1}(p_L - p_m) \tag{56}$$

Combining this relation linking p_R to p_L with Eq. (54), an expression of p_L as a function of the material parameters is obtained:

$$p_L = p_m\sqrt{1 - \frac{H_1}{H_2}} \tag{57}$$

Combining then Eqs. (55) and (57), the following decomposition is derived:

$$\underbrace{p_L(\sigma_p - \sigma_m)}_{A_{Lud}} = \underbrace{\frac{p_m(\sigma_M - \sigma_m)}{2}}_{A^1_{Loc}} + \underbrace{\frac{(p_L - p_m)(\sigma_p - \sigma_m)}{2}}_{A^2_{Loc}} \tag{58}$$

The left-hand side represents the part of the total plastic work in excess to $\sigma_m p_L$. The Fig. 8 illustrates this relation and shows that the first term in the right-hand side corresponds to the plastic work below the softening branch of the function $R(p)$, whereas the second term denotes the plastic work in the hardening regime until the plastic strain p_L is reached. The relation (58) therefore means that the total plastic work per unit volume experienced by the whole sample (overall response with a plateau) is equal to the plastic work experienced by each individual material point after the passage of the band. This is strictly equivalent to the Maxwell construction presented above.

4.4 Analytical solution for plastic strain rate $\dot{p}$

In order to compare the results with finite element solutions, Eq. (37) is differentiated with respect to time to obtain its rate form. The evolution of the cumulative plastic strain rate is computed in the band front and band tail, and at the interface $Y = 0$.

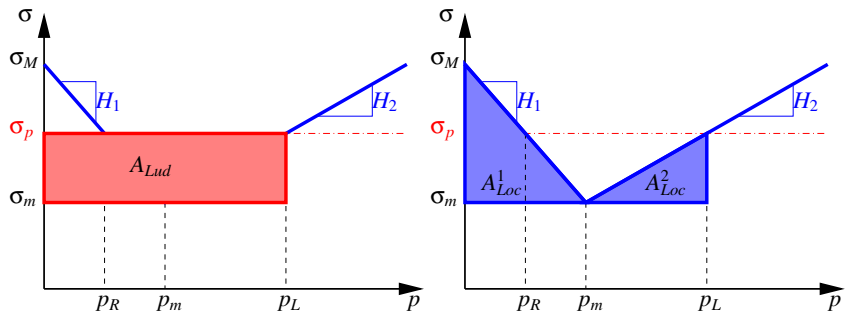

Fig. 8 Representation of the relationship between the constitutive hardening law and Lüders plateau provided by Eq. (58). This relation is equivalent to Maxwell's equal area rule

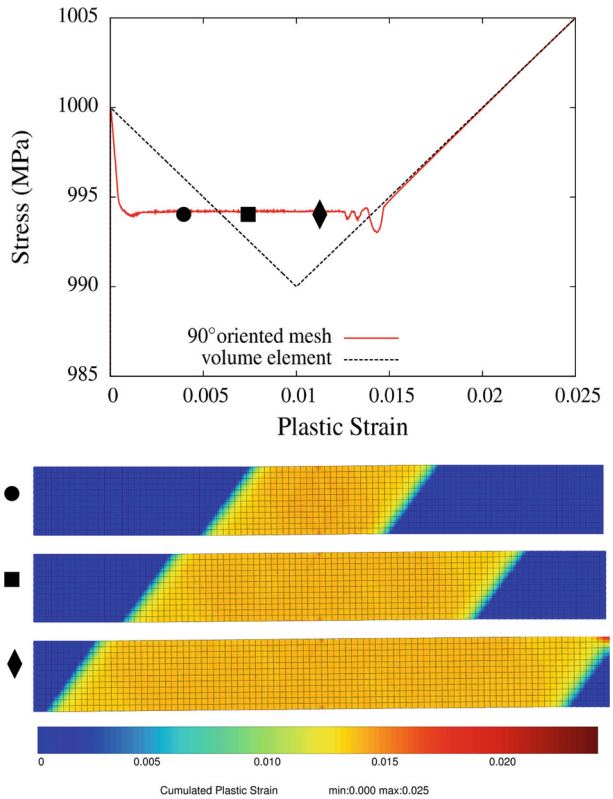

Fig. 9 Overall stress versus plastic strain curve for the 90° oriented mesh using the strain gradient plasticity model. Maps of the local cumulative plastic strain for a global plastic strain equal to 0.004 (*bullet*), 0.008 (*black square*), and 0.012 (*black diamond*)

Solution in the band tail

The problem is similar to the one investigated in Sect. 4.2. In the band tail, the rate form of Eq. (40) becomes:

$$\dot{p}'' - w_2^2\,\dot{p} = 0 \Longrightarrow \dot{p}(Y) = \dot{p}_0 \exp(w_2 Y) \tag{59}$$

where $\dot{p}_0 = \dot{p}(0)$ is the plastic strain rate at the interface $Y = 0$. This value $\dot{p}_0$ depends on the overall prescribed plastic strain rate $\dot{\varepsilon}^p$ and will be calculated hereafter.

Solution in the band front

In the band front, the rate form of Eq. (40) becomes

$$\dot{p}'' + w_1^2\,\dot{p} = 0 \Longrightarrow \dot{p}(Y) = \dot{p}_0(\cos(w_1 Y) + \frac{w_2}{w_1}\sin(w_1 Y)) \tag{60}$$

after making use of the continuity condition of $\dot{p}$ and $\dot{p}'$ at $Y = 0$. Moreover, it can be checked that $\dot{p}(Y_f) = 0$.

Evaluation of $\dot{p}_0$

The cumulative plastic strain rate at the interface between band front and band tail can be evaluated using the global prescribed plastic strain rate $\dot{\varepsilon}^p$. The displacement rate $\dot{u}$ of a specimen of length L can be computed as the sum of local plastic strain rate contributions (the elastic strain rate contribution vanishes as long as $\sigma = \sigma_p$):

$$\dot{u} = L\dot{\varepsilon}^p_{22} = \int_{-\infty}^{+\infty} \dot{p}\,\mathrm{d}Y \tag{61}$$

from which we obtain, taking the previously derived distribution of $\dot{p}$:

$$\dot{p}_0 = \frac{L\dot{\varepsilon}^p}{L_b^{eq}} \tag{62}$$

with

$$L_b^{eq} = \sqrt{-\frac{A}{H_1}}\left(\sqrt{-\frac{H_2}{H_1}} + \sqrt{-\frac{H_1}{H_2}}\right)\left(1 + \frac{1}{\sqrt{1 - \dfrac{H_1}{H_2}}}\right) \tag{63}$$

This equivalent width L_b^{eq} represents the width of a band that would carry all the plastic strain rate at a constant level equal to $\dot{p}_0$.

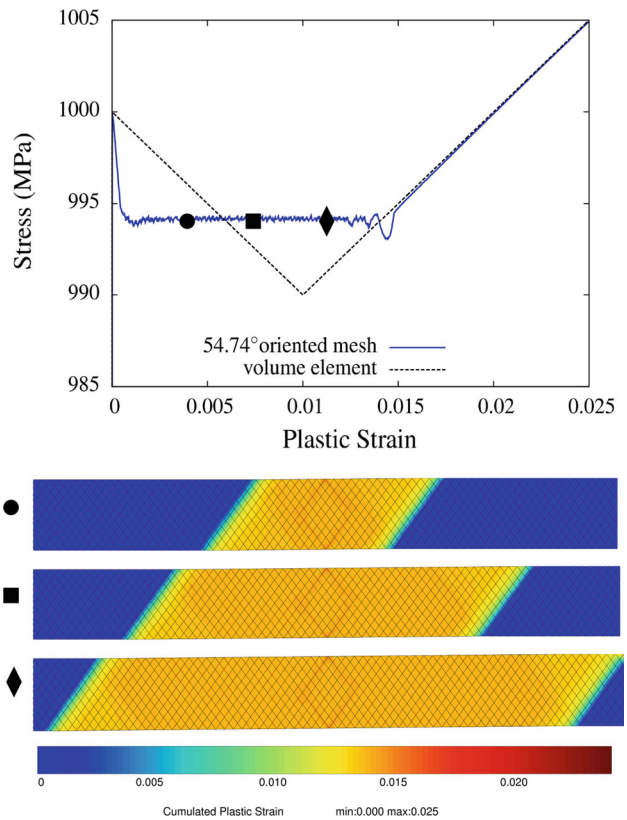

Fig. 10 Global stress versus plastic strain curve for the 54.74° oriented mesh using the regularized model. Maps of the local cumulative plastic strain for a global plastic strain equal to 0.004 (*bullet*), 0.008 (*black square*), and 0.012 (*black diamond*)

5 Comparison with finite element simulations

The derived analytical solution for a single propagating band in an elastoplastic strain gradient medium can now be used to validate the regularization method proposed in Sect. 3 for the finite element simulation of Lüders band formation and propagation in a metal plate, as done in Sect. 2.

The strain gradient plasticity model is used with the following value of the additional material parameter

$$A = 1000 \text{ MPa mm}^2$$

With this value, and those of the plastic moduli $H_1 = -1{,}000$ MPa, and $H_2 = 1{,}000$ MPa, the band front thickness is

$$Y_f = 2.35 \text{ mm}$$

and the equivalent band width is $L_b^{eq} = 3.41$ mm. These values are small compared to the specimen size (96 mm length, 12 mm width) but large compared to the element size (1 mm, 9 integration points in each quadratic element).

The simulation on the 90° oriented 2D mesh using the regularized model is presented in Fig. 9. The overall curve is close to the one obtained using conventional plasticity, see Fig. 3. The plateau level is around $\sigma_p = 994$ MPa close to the analytical value calculated using Eq. (55).

The simulation on the 54.74° oriented 2D mesh using the regularized model is presented in Fig. 10. Results strongly differ from that obtained with conventional plasticity, see Fig. 4. The overall stress does not oscillate and follows a plateau at the same level as obtained for the 90° oriented mesh (~ 994 MPa). The maps of

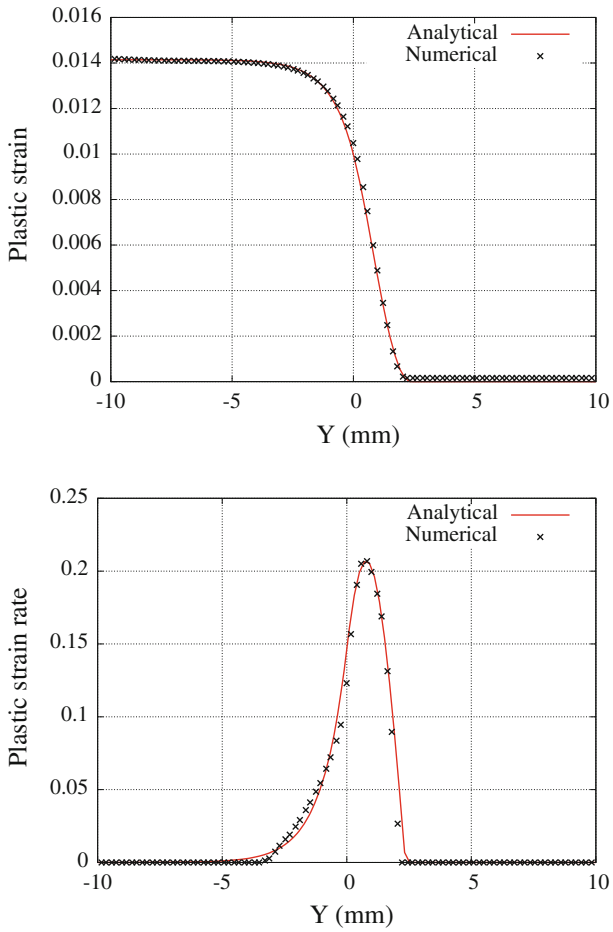

Fig. 11 Analytical and numerical evolutions of the cumulative plastic strain p and strain rate $\dot{p}$ along a line parallel to the tensile direction, as a function of the coordinate Y in the local frame associated with the band

cumulative plastic strain at three different levels are the same for both meshes. Complementing computations provided in [44] show that the results do not depend on mesh either and that convergence is reached when at least 5 elements lie in the band front. The strain gradient plasticity model therefore provides mesh-independent simulations of the Lüders band propagation. It can also be noted that the crossing of multiple bands that were observed in the simulations based on classical elastoplasticity, see Fig. 3, does not occur in the regularized simulations. Instead, a single band is traveling through the sample. Multiple bands can also be observed in some simulations but the finite extent of the band front limits the number of bands.

The profiles of the cumulative plastic strain p and strain rate $\dot{p}$ have been extracted along a line parallel to the tensile direction at the middle of the specimen from the simulation on the 54.74° oriented 2D mesh using the regularized model for a global plastic strain equal to 0.008. The comparison with analytical results is plotted in Fig. 11(top) for the profile of plastic strain. The numerical results are in perfect agreement with the analytical solution. The band front width Y_f and the plastic strain far behind the band front p_L are correctly described. The same comparison is drawn for the plastic strain rate profile in Fig. 11(bottom). Excellent agreement is reached again. Slight differences are observed due to the fact that the strain rate is extremely sensitive to the exact scenario of localization along the X direction. Better agreement is found for even finer meshes.

6 Conclusions

A simple strain gradient plasticity framework was proposed that is appropriate for the simulation of Lüders band initiation and propagation in isotropic metals. A detailed analysis of the plastic strain distribution developing in a finite width band front and behind was given both theoretically and numerically. Exact expressions of the plateau stress, the Lüders stress, and the band front width allow for a direct identification of material parameters from the overall curves from which σ_p and p_L are deduced and from strain field measurements with sufficient resolution for the determination of the band front behavior. The proposed elastoplastic regularized model has 5 independent parameters: σ_M, σ_m, H_1, H_2, A. The experimental peak stress value is used to identify parameter σ_M. The hardening behavior beyond Lüders plateau provides the complete information on the hardening part of the local law (H_2 and indirectly σ_m). The Lüders plateau stress level and the experimental band front size are then used to identify H_1 and A using the analytical expressions proposed in this work. The set of parameters is then unique and easy to obtain. This identification method can even be extended to nonlinear hardening or viscoplastic behavior as done in [44]. The analytical solution presented in this work then provides useful estimations of the material parameters that have to be used in the more sophisticated model from [44] or related ones.

The mesh sensitivity of conventional finite element simulations of the Lüders behavior has often been overlooked in the literature. The strong dependence on the relative orientation between element edges and loading direction has been evidenced and suppressed by means of the strain gradient plasticity approach. The mesh sensitivity is much more pronounced for plane stress finite element simulations than for 3D specimens but the effect is still present in the latter case especially for thin specimens. Some first results of 3D simulations based on the strain gradient plasticity model for the propagation of Lüders bands in cylindrical specimens are given in [44].

The propagation of strain localization bands is an ubiquitous phenomenon in plasticity of complex materials and soils. In metallic foams for instance, crushing bands form due to the collapse of one cell row and propagate due to the densification-induced hardening inside the band. A plateau regime is also observed on the overall curve. The strain gradient plasticity approach can be extended to pressure-dependent plasticity as done for instance in [24,61] for aluminum foams. More generally, boundary layers develop in microstructured solids like foams or textile materials, as shown in [19] where a micromorphic model was used to account for shear boundary layers.

Another perspective of the present work is a better understanding of the deformation processes at work in the band front for instance by means of a microstructure-based description of localization. What is the link between macroscopic localization and plastic slip processes at work inside the grains. Coupling crystal plasticity and strain aging was considered in [35]. Such an approach could be extended to Lüders behavior and strain gradient crystal plasticity [11].

Acknowledgments The authors would like to acknowledge the scientific and financial support from Electricité de France (EdF Les Renardières). Anthony Marais, Aurore Parrot, and Patrick Le-Delliou are also acknowledged for helpful discussions.

Appendix: Micromorphic plasticity model

The objective of this Appendix is to provide the micromorphic plasticity model implemented in the finite element code Zset and used for the simulations of Lüders band propagation presented in this work. It is shown that the strain gradient plasticity model detailed in Sect. 3 arises as a special limiting case of the micromorphic model.

The starting point is the classical elastoplastic non-regularized model described in Sect. 2.1. In the micromorphic extension of this classical model, a new degree of freedom, p_χ, is introduced, which has the physical meaning of a plastic microdeformation (see [21,22] for a more detailed presentation of the micromorphic approach to gradient plasticity). This additional DOF p_χ is to be compared to the cumulative plastic strain p. Under homogeneous loading conditions, we will have $p_\chi = p$, whereas the plastic microdeformation can differ from p in the presence of strong strain gradients. The mechanical power density of internal forces is extended in the form

$$p^{(i)}(\dot{\underset{\sim}{\boldsymbol{\varepsilon}}}, \dot{p}_\chi) = \underset{\sim}{\boldsymbol{\sigma}} : \dot{\underset{\sim}{\boldsymbol{\varepsilon}}} + a\,\dot{p}_\chi + \underline{\boldsymbol{b}} \cdot \nabla \dot{p}_\chi \tag{64}$$

where generalized stresses a and $\underline{\boldsymbol{b}}$ are introduced, which are similar to the microforces and microstresses in Gurtin's theory [31]. The free energy density function is assumed to depend on the elastic strain, the cumulative plastic strain, the plastic microdeformation, and its gradient in the form:

$$\psi(\underset{\sim}{\boldsymbol{\varepsilon}}_e, p, p_\chi, \nabla p_\chi) = \frac{1}{2}\underset{\sim}{\boldsymbol{\varepsilon}}^e : \underset{\sim}{\underset{\sim}{\boldsymbol{E}}} : \underset{\sim}{\boldsymbol{\varepsilon}}^e + \psi_p(p) + \psi_\chi(p, p_\chi, \nabla p_\chi) \tag{65}$$

where ψ_p is the classical stored energy by means of dislocations related to p and ψ_χ is the additional micromorphic contribution. A simple quadratic potential is adopted for the latter:

$$\psi_\chi(p, p_\chi, \nabla p_\chi) = H_\chi(p - p_\chi)^2 + \frac{1}{2}\nabla p_\chi \cdot \underset{\sim}{\boldsymbol{A}} \cdot \nabla p_\chi \tag{66}$$

where the generalized moduli H_χ (unit MPa) and $\underset{\sim}{\boldsymbol{A}}$ (unit MPa.mm^2) are new material parameters.

The state laws are obtained after differentiating the free energy potential:

$$\underset{\sim}{\boldsymbol{\sigma}} = \frac{\partial \psi}{\partial \underset{\sim}{\boldsymbol{\varepsilon}}^e} = \underset{\sim}{\underset{\sim}{\boldsymbol{E}}} : \underset{\sim}{\boldsymbol{\varepsilon}}^e \tag{67}$$

$$R = \frac{\partial \psi}{\partial p} = \frac{\partial \psi_p}{\partial p} + H_\chi(p - p_\chi) \tag{68}$$

$$a = \frac{\partial \psi}{\partial p_\chi} = -H_\chi(p - p_\chi) \tag{69}$$

$$\underset{\sim}{\boldsymbol{b}} = \frac{\partial \psi}{\partial \nabla p_\chi} = \underset{\sim}{\boldsymbol{A}}.\nabla p_\chi \tag{70}$$

The variable R represents the hardening function. It is composed of a first part $\partial \psi_p / \partial p$, which is taken identical to $R(p)$ given by Eqs. (6) and (7), and an additional part involving the new degree of freedom and its gradient.

The classical and generalized stress tensors must fulfill two balance equations [21]:

$$\operatorname{div} \underset{\sim}{\boldsymbol{\sigma}} = 0, \quad \operatorname{div} \underline{\boldsymbol{b}} - a = 0 \tag{71}$$

in the absence of body forces and in the static case. The balance equations must be complemented by traction conditions in the form

$$\underset{\sim}{\boldsymbol{\sigma}} \cdot \underline{\boldsymbol{n}} = \underline{\boldsymbol{t}}, \quad \underline{\boldsymbol{b}} \cdot \underline{\boldsymbol{n}} = a_c \tag{72}$$

for all points lying at the boundary of the body with normal vector $\underline{\boldsymbol{n}}$. The traction vector $\underline{\boldsymbol{t}}$ is the surface density of applied forces and a_c is a generalized traction associated with the additional degree of freedom.

When inserted in the additional balance equation linking a and $\underline{\boldsymbol{b}}$, the state laws (67) to (70) lead to the following partial differential equation

$$p_\chi - \frac{1}{H_\chi}\operatorname{div}(\underset{\sim}{\boldsymbol{A}}.\nabla p_\chi) = p \tag{73}$$

This equation is now specialized to the case of isotropic materials, for which the second-order tensor of micromorphic stiffness reduces to $\underset{\sim}{\boldsymbol{A}} = A\underset{\sim}{\mathbf{1}}$, which involves a single additional material parameter. Equation (73) then becomes

$$p_\chi - l_c^2 \nabla^2 p_\chi = p, \quad \text{with} \quad l_c^2 = \frac{A}{H_\chi} \tag{74}$$

where l_c is a characteristic length of the model. This diffusive partial differential equation is the same as the one proposed in [18,51,53] for the regularization of softening plasticity or damage phenomena.

As a result, the hardening function can also be written

$$R = R(p) - A\nabla^2 p_\chi \tag{75}$$

The material parameter H_χ can also be seen as a penalty coefficient that forces the relative plastic strain $e = p - p_\chi$ to remain small. It can be shown that a high value of H_χ keeps e close to zero. In that case, the plastic microdeformation p_χ in the hardening law (75) can be replaced by p itself:

$$R = R(p) - A\nabla^2 p \tag{76}$$

which is exactly Aifantis strain gradient plasticity model [1]. In that case, there is one single new material parameter, namely A. In the case of the elastoplastic material model presented in Sect. 2.1, plastic yielding occurs when the yield criterion is reached and then

$$\sigma_{\text{eq}} = \sigma_M + R(p) - A\nabla^2 p \tag{77}$$

which is the same as (37).

The numerical implementation of this model follows the standard of conventional nonlinear mechanical models. Quadratic elements are used with three degrees of freedom per node (u_1, u_2, p_χ). Global equilibrium is solved using an implicit Newton algorithm, and the differential constitutive equations at Gauss points are integrated by means of an implicit θ-method [7].

References

1. Aifantis, E.: On the microstructural origin of certain inelastic models. J. Eng. Mater. Technol. **106**, 326–330 (1984)
2. Aifantis, E.C.: The physics of plastic deformation. Int. J. Plasticity **3**, 211–248 (1987)
3. Anand, L., Aslan, O., Chester, S.: A large-deformation gradient theory for elastic–plastic materials: strain softening and regularization of shear bands. Int. J. Plasticity **30–31**, 116–143 (2012)
4. Ballarin, V., Perlade, A., Lemoine, X., Bouaziz, O., Forest, S.: Mechanisms and modeling of bake-hardening steels: Part II. Complex loading paths. Metall. Mater. Trans. A **40**, 1367–1374 (2009)
5. Ballarin, V., Soler, M., Perlade, A., Lemoine, X., Forest, S.: Mechanisms and modelling of bake-hardening steels: Part I. Uniaxial tension. Metall. Mater. Trans. **40**, 1367–1374 (2009)
6. Belotteau, J., Berdin, C., Forest, S., Parrot, A., Prioul, C.: Mechanical behavior and crack tip plasticity of a strain aging sensitive steel. Mater. Sci. Eng. A **526**(1–2), 156–165 (2009)
7. Besson, J., Cailletaud, G., Chaboche, J.L., Forest, S.: Non Linear Mechanics of Materials. Springer, Berlin (2009)
8. Besson, J., Foerch, R.: Large scale object-oriented finite element code design. Comput. Meth. Appl. Mech. Eng. **142**, 165–187 (1997)
9. de Borst, R., Sluys, L., Mühlhaus, H., Pamin, J.: Fundamental issues in finite element analyses of localization of deformation. Eng. Comput. **10**, 99–121 (1993)
10. Butler, J.F.: Lüders front propagation in low carbon steels. J. Mech. Phys. Solids **10**, 313–334 (1962)
11. Cordero, N.M., Forest, S., Busso, E.P.: Generalised continuum modelling of grain size effects in polycrystals. Comptes Rendus Mécanique **340**, 261–274 (2012)
12. Cottrell, A.H., Bilby, B.A.: Dislocation theory of yielding and strain ageing of iron. Proc. Phys. Soc. A **62**(1), 49–62 (1949)
13. Dell'Isola, F., Seppecher, P.: The relationship between edge contact forces, double forces and intersticial working allowed by the principle of virtual power. C.R. Acad. Sci. Paris IIb **321**, 303–308 (1995)
14. Dell'Isola, F., Seppecher, P., Madeo, A.: How contact interactions may depend on the shape of Cauchy cuts in N-th gradient continua: approach "la D'Alembert". Zeitschrift Fr Angewandte Mathematik Und Physik **63**, 1119–1141 (2012)
15. Dimitrijevic, B., Hackl, K.: A regularization framework for damage plasticity models via gradient enhancement of the free energy. Int. J. Numer. Meth. Biomed. Eng. **27**, 1199–1210 (2011)
16. Dingley, D.J., McLean, D.: Components of the flow stress of iron. Acta Metall. **15**, 885–901 (1967)
17. Enakoutsa, K., Leblond, J.: Numerical implementation and assessment of the GLPD micromorphic model of ductile rupture. Eur. J. Mech. A/Solids **28**, 445–460 (2009)
18. Engelen, R., Geers, M., Baaijens, F.: Nonlocal implicit gradient-enhanced elasto-plasticity for the modelling of softening behaviour. Int. J. Plasticity **19**, 403–433 (2003)

19. Ferretti, M., Madeo, A., Dell'Isola, F., Seppecher, P., Boisse, P.: Modeling the onset of shear boundary layers in fibrous composite reinforcements by second-gradient theory. Zeitschrift für Angewandte Mathematik und Physik (2013)
20. Forest, S.: Strain localization phenomena in generalized crystal plasticity. In: Second Euroconference and International Symposium on Material Instabiblities in Deformation and Fracture, Journal of the Mechanical Behavior of Materials, vol. 11, pp. 45–50. organized by E.C. Aifantis, Aristotle Technical University, Thessaloniki, Greece (1997)
21. Forest, S.: Micromorphic approach for gradient elasticity, viscoplasticity, and damage. J. Eng. Mech. **135**(3), 117–131 (2009)
22. Forest, S., Aifantis, E.C.: Some links between recent gradient thermo-elasto-plasticity theories and the thermomechanics of generalized continua. Int. J. Solids Struct. **47**, 3367–3376 (2010)
23. Forest, S., Bertram, A. : Formulations of strain gradient plasticity. In: Altenbach, H., Maugin, G.A., Erofeev, V. (eds.) Mechanics of Generalized Continua, Advanced Structured Materials, Vol. 7, pp. 137–150. Springer, Berlin (2011)
24. Forest, S., Blazy, J., Chastel, Y., Moussy, F.: Continuum modelling of strain localization phenomena in metallic foams. J. Mater. Sci. **40**, 5903–5910 (2005)
25. Forest, S., Sievert, R.: Elastoviscoplastic constitutive frameworks for generalized continua. Acta Mech. **160**, 71–111 (2003)
26. Fressengeas, C., Beaudoin, A., Lebyodkin, M., Kubin, L., Estrin, Y.: Dynamic strain aging: a coupled dislocation-solute dynamic model. Mater. Sci. Eng. **51**, 226–230 (2005)
27. Germain, P.: La méthode des puissances virtuelles en mécanique des milieux continus, première partie: théorie du second gradient. J. de Mécanique **12**, 235–274 (1973)
28. Germain, P.: The method of virtual power in continuum mechanics. part 2: Microstructure. SIAM J. Appl. Math. **25**, 556–575 (1973)
29. Graff, S., Forest, S., Strudel, J.L., Prioul, C., Pilvin, P., Béchade, J.L.: Strain localization phenomena associated with static and dynamic strain ageing in notched specimens: experiments and finite element simulations. Mater. Sci. Eng. A **387–389**: 181–185 (2004)
30. Graff, S., Forest, S., Strudel, J.L., Prioul, C., Pilvin, P., Béchade, J.L.: Finite element simulations of dynamic strain ageing effects at V-notches and crack tips. Scripta Materialia **52**, 1181–1186 (2005). doi:10.1016/j.scriptamat.2005.02.007
31. Gurtin, M.: On a framework for small-deformation viscoplasticity: free energy, microforces, strain gradients. Int. J. Plasticity **19**, 47–90 (2003)
32. Hähner, P.: Modelling the spatio-temporal aspects of the Portevin–Le Chatelier effect. Mater. Sci. Eng. A **164**, 23–34 (1993)
33. Hähner, P., Kubin, L.P.: Coherent propagative structures in plastic deformation: a theory of lüders bands in polycrystals. Solid State Phenomena **23–24**, 385–402 (1992)
34. Kochmann, D., Hackl, K.: The evolution of laminates in finite crystal plasticity: a variational approach. Contin. Mech. Thermodyn. **23**, 65–85 (2011)
35. Kok, S., Bharathi, M., Beaudoin, A., Fressengeas, C., Ananthakrishna, G., Kubin, L., Lebyodkin, M.: Spatial coupling in jerky flow using polycristal plasticity. Acta Materialia **51**, 3651–3662 (2003)
36. Kubin, L., Estrin, Y.: The Portevin–Le Chatelier effect in deformation with constant stress rate. Acta Mater. **33**, 397–407 (1985)
37. Kyriakides, S., Miller, J.E.: On the propagation of Lüders bands in steel strips. J. Appl. Mech. **67**, 645–654 (2000)
38. Lambrecht, M., Miehe, C., Dettmar, J.: Energy relaxation of non-convex incremental stress potentials in a strain-softening elastic–plastic bar. Int. J. Solids Struct. **40**(6), 1369–1391 (2003)
39. Liebe, T., Menzel, A., Steinmann, P.: Theory and numerics of geometrically non-linear gradient plasticity. Int. J. Eng. Sci. **41**, 1603–1629 (2003)
40. Liebe, T., Steinmann, P., Benallal, A.: Theoretical and computational aspects of a thermodynamically consistent framework for geometrically linear gradient damage. Comp. Methods Appl. Mech. Eng. **190**, 6555–6576 (2001)
41. Lomer, W.M.: The yield phenomenon in polycrystalline mild steel. J. Mech. Phys. Solids **1**, 64–73 (1952)
42. Louche, H., Chrysochoos, A.: Thermal and dissipative effects accompanying Lüders band propagation. Mater. Sci. Eng. **307**, 15–22 (2001)
43. Lüders, W.: Über die Äusserung der Elasticität an stahlartigen Eisenstäben und Stahlstäben, und über eine beim Biegen solcher Stäbe beobachtete Molecularbewegung. Dinglers Polytech J **5**, 18–22 (1860)
44. Marais, A., Mazière, M., Forest, S., Parrot, A., Le Delliou, P.: Identification of a strain-aging model accounting for lüders behavior in a c-mn steel. Philos. Mag. **92**(28–30), 3589–3617 (2012)
45. Maxwell, J.: On the dynamical evidence of the molecular constitution of bodies. Nature **11**, 357–359 (1875)
46. Mazière, M., Besson, J., Forest, S., Tanguy, B., Chalons, H., Vogel, F.: Numerical aspects in the finite element simulation of the Portevin–Le Chatelier effect. Comp. Method Appl. Mech. Eng. **199**, 734–754 (2010)
47. McCormick, P.G.: Theory of flow localization due to dynamic strain ageing. Acta Metall. **36**, 3061–3067 (1988)
48. Mesarovic, S.: Dynamic strain aging and plastic instabilities. J. Mech. Phys. Solids **43**(5), 671–700 (1995)
49. Mindlin, R., Eshel, N.: On first strain gradient theories in linear elasticity. Int. J. Solids Struct. **4**, 109–124 (1968)
50. Mühlhaus, H.B., Boland, J.: A gradient plasticity model for Lüders band propagation. Pure Appl. Geophys. **137**(4), 391–407 (1991)
51. Peerlings, R., Poh, L., Geers, M.: An implicit gradient plasticity-damage theory for predicting size effects in hardening and softening. Eng. Fract. Mech. **95**, 2–12 (2012)
52. Piobert, G.: Expérience sur la pénétration des projectiles dans le fer forgé. Mémoire de l'Artillerie, p. 505 (1842)
53. Poh, L., Peerlings, R., Geers, M., Swaddiwudhipong, S.: An implicit tensorial gradient plasticity model—formulation and comparison with a scalar gradient model. Int. J. Solids Struct. **48**, 2595–2604 (2011)
54. Rice, J.: The localisation of plastic deformation. In: Koiter, W. (ed.) Proceedings of 14th International Conference Theoretical and Applied Mechanics. Delft, North–Holland, Amsterdam, pp. 207–220 (1976)
55. Soler, M.: Etude du vieillissement d'un acier à bake hardening: évolution des propriétés mécaniques de traction—corrélation avec la microstructure. Ph.D. thesis, INSA Lyon (1998)
56. Tsukahara, H., Iung, T.: Finite element simulation of the Piobert-lüders behavior in an uniaxial test. Mater. Sci. Eng. A **248**, 304–308 (1998)

57. Tsukahara, H., Iung, T.: Piobert–Lüders and Portevin–Le Chatelier instabilities. finite element modelling with abaqus. J. Phys. IV **9**, 157–164 (1999)
58. Wang, H.D., Berdin, C., Mazière, M., Forest, S., Prioul, C., Parrot, A., Le-Delliou, P.: Portevin–Le Chatelier (PLC) instabilities and slant fracture in C-Mn steel round tensile specimens. Scrypta Mater. **64**, 430–433 (2011)
59. Wenman, M.R., Chard-Tuckey, P.R.: Modelling and experimental characterisation of the Lüders strain in complex loaded ferritic steel compact tension specimens. Int. J. Plasticity **26**, 1013–1028 (2010)
60. Wulfinghoff, S., Böhlke, T.: Equivalent plastic strain gradient enhancement of single crystal plasticity: theory and numerics. Proc. R. Soc. A **468**, 2682–2703 (2012)
61. Zaiser, M., Mill, F., Konstantinidis, A., Aifantis, K.: Strain localization and strain propagation in collapsible solid foams. Mater. Sci. Eng. A **567**, 38–45 (2013)